J Nanopart Res (2014) 16:2791
DOI 10.1007/s11051-014-2791-6

RESEARCH PAPER

Relaxation time diagram for identifying heat generation mechanisms in magnetic fluid hyperthermia

Enio Lima Jr. · Emilio De Biasi · Roberto D. Zysler · Marcelo Vasquez Mansilla · Mary L. Mojica-Pisciotti · Teobaldo E. Torres · M. Pilar Calatayud · C. Marquina · M. Ricardo Ibarra · Gerardo F. Goya

Received: 3 September 2014 / Accepted: 1 December 2014

Abstract We present a versatile diagram to envisage the dominant relaxation mechanism of single-domain magnetic nanoparticles (MNPs) under alternating magnetic fields, as those used in magnetic fluid hyperthermia (MFH). The diagram allows estimating the heating efficiency, measured by the Specific Power Absorption (SPA), originated in the magnetic and viscous relaxation times of single-domain MNPs for a given frequency of the ac magnetic field (AFM). The diagram has been successfully applied to different colloids, covering a wide variety of MNPs with different magnetic anisotropy and particle size, and dispersed in different viscous liquid carriers. From the general diagram, we derived a specific chart based on the Linear Response Theory in order to easily estimate the experimental condition for the optimal SPA values of most colloids currently used in MFH.

Keywords Magnetic hyperthermia · Magnetic losses · Néel relaxation · Brown relaxation · Nanoparticles · Specific power absorption · Superparamagnetism

Introduction

Magnetic fluid hyperthermia (MFH) also known as magnetic thermotherapy is currently being used in clinics as a technique for cancer treatment, either alone or in combination with chemo- and radio-therapy (Maier-Hauff et al. 2007). MFH consists in locally generating heat in a target tissue, previously loaded with magnetic nanoparticles (MNPs), by applying alternating magnetic fields (AMF) to the tissue. There are limitations on the use of MNPs to generate heat from AMFs in biomedicine, based on physiological considerations that

E. Lima Jr. (✉) · E. De Biasi · R. D. Zysler · M. Vasquez Mansilla · M. L. Mojica-Pisciotti
Centro Atómico Bariloche/CONICET, CP 8400, San Carlos de Bariloche, Rio Negro, Argentina
e-mail: lima@cab.cnea.gov.ar

E. De Biasi · R. D. Zysler · M. L. Mojica-Pisciotti
Instituto Balseiro, CP 8400, San Carlos de Bariloche, Rio Negro, Argentina

T. E. Torres · M. P. Calatayud · C. Marquina · M. Ricardo Ibarra · G. F. Goya
Instituto de Nanociencia de Aragón INA, Universidad de Zaragoza, 50018 Saragossa, Spain

T. E. Torres · M. Ricardo Ibarra
Laboratorio de Microscopías Avanzadas LMA, Universidad de Zaragoza, 50018 Saragossa, Spain

T. E. Torres · M. P. Calatayud · M. Ricardo Ibarra · G. F. Goya
Departamento de Física de la Materia Condensada, Universidad de Zaragoza, 500018 Saragossa, Spain

C. Marquina
Instituto de Ciencia de Materiales de Aragón, CSIC - Universidad de Zaragoza, Saragossa, Spain

Published online: 23 December 2014

suggest that the delivered power should be limited in the amplitude H_0 and frequency f, through the limit product value of f. $H_0 = 4.85 \times 10^8$ *A/m.s* (Brezovich 1988). Despite these limitations, MFH has many advantages related to the ability of preserving healthy surrounding tissues by locally heating the cancer cells that absorb or are in contact with MNPs (the heating agents). It is thus clear the need of a tool for foreseeing the requirements of the magnetic materials that can respond with maximum efficiency within the acceptable range of f and H_0.

The heating efficiency of a colloid in a MFH experiment is measured by the specific power absorption (SPA), which is the capability to absorb the radio-frequency power by the nanoparticles and the subsequent conversion into heat. The SPA values measured for a ferrofluid containing magnetic nanoparticles exposed to a AMF with given f and H_0 are strongly dependent on the magnetic, morphological, and rheological properties of the system, specifically to the saturation magnetization (M_S), the effective anisotropy (K_{eff}), the magnetic volume (V_{mag}), the viscosity of the liquid (η), and the hydrodynamic volume (V_{hyd}). It is imperative to understand the heating mechanism acting in the MFH experiment to optimize the SPA for different experimental conditions.

For single-domain MNPs in the presence of AMF with moderated f and H_0, the magnetic loss is promoted by the delay between applied field and magnetic moment of the system (Usov and Liubimov 2012). The relaxation of magnetic moment is usually modeled with two mechanisms (Laurent et al. 2011), the Brown relaxation process associated with the physical rotation of the whole nanoparticle in the fluid (Brown relaxation time), and the magnetic one related to the fluctuation of magnetization through the magnetic energy barrier (Néel relaxation time). Brown relaxation time depends on the rheological properties of the system and can be calculated as $\tau_B = 3\eta V_{hyd}/k_BT$, where η is the viscosity of the liquid, V_{hyd} is the hydrodynamic volume of the nanoparticles, and k_BT is the thermal energy. Néel relaxation time depends on the magnetic properties and it is given by $\tau_N = \tau_0 exp(K_{eff}V_{mag}/k_BT)$, where V_{mag} is the volume of the magnetic single-domain nanoparticle (*magnetic volume*), K_{eff} is the effective anisotropy of the magnetic single-domain, and τ_0 is the characteristic relaxation time (10^{-9}–10^{-11} *s*). The value of $K_{eff}V_{mag}$ represents the anisotropy energy barrier in the case of non-interacting nanoparticles. Both mechanisms take place simultaneously in the system; however, they depend on different parameters: τ_B is proportional to the hydrodynamic volume and viscosity while τ_N depends exponentially on the anisotropy and the magnetic volume of the particle.

In the literature, several models are presented looking for the optimization of the SPA of magnetic nanoparticles considering the two heating mechanisms discussed above. Rosensweig (2002) proposed a model where both Neel relaxation ("*magnetic mechanism*") and Brown relaxation ("*viscous mechanism*") are taken into account as independent mechanisms that take place in parallel. The proposed effective relaxation time is $\tau_{eff}^{-1} = \tau_B^{-1} + \tau_N^{-1}$, but the use of τ_{eff} is not completely justified since it assumes that magnetic and mechanical relaxation mechanisms are independent. This assumption is not true, however, the functions of the relaxation times present continuity, and the incongruence in the definition of τ_{eff} takes importance only in the region where both relaxation times have similar values, a delimited region in terms of diameters of the nanoparticles. From this expression of τ_{eff}, the SPA is calculated with using the Linear Response Theory (LRT). The Rosensweigś model is valid only for the region where the LRT is valid, *i.e.*, when the magnetization response to the applied field is linear (Haiwen Xi et al. 2006).

Carrey et al. (2011) have performed calculations of the SPA to describe the case where only Néel relaxation is relevant, proposing the approximation of the minor hysteresis loop area to an elliptical area in order to estimate the SPA value of such a system. Recently, Usov and Liubimov (2012) and Mamiya and Jeyadevan (2011) calculated numerically the hysteresis loop produced by a system of single-domain NPs under an ac magnetic field, taking into account both Néel and Brown magnetic relaxation mechanisms. Usov and Liubimov (2012) coined the terms *viscous mode* and *magnetic mode* to identify the situations where the Brown relaxation or Neel relaxation is the dominant mechanism, respectively. These two modes were defined by the ratio between the applied field H_0 to the anisotropy field H_K. These theoretical models for the SPA in magnetic fluids represent a clear advancement in the understanding of the physics of magnetic single-domains under AMFs, and also of the complex relationship between magnetic, rheological, and thermal parameters. However, there is still an

increasing need for a comprehensive landscape that compiles the theoretical output from these models and translates them into the expected behavior regarding heat generation in MFH. Such a tool would be helpful for a non-specialist in magnetism working on MFH for identifying the actual relaxation mechanism for a given type of sample and experimental conditions. It could be helpful to find the predicted SPA value in that situation, and consequently foretelling the heat generation efficiency expected for that sample in a given in vivo or in vitro MFH experiments.

In this work, we propose a versatile diagram to identify the dominant heating mechanism of magnetic single-domains in MFH, based on the previous knowledge of the physical parameters involved in the magnetic relaxation times: magnetic anisotropy, liquid viscosity, hydrodynamic particle volume, and the "*magnetic diameter*". Working as a 'phase diagram', it indicates the dominant heating mechanism through the relaxation times τ_N and τ_B of the magnetic single-domain at the condition of H_0, f of the applied AMF. Thus, it can predict the expected heating mechanism of a ferrofluid in a MFH experiment on the bases of the important parameters of the system, specifically K_{eff}, V_{mag}, η, and V_{hyd}. Once we know the dominant mechanism, an appropriate model or theory can be used to calculate the expected SPA value of this system. We tested this diagram by predicting the main heating mechanism and the experimental SPA values of six ferrofluids containing ferrite nanoparticles hydrophobic and hydrophilic Fe_3O_4, $NiFe_2O_4$, and $CoFe_2O_4$ systems. Finally, we built a second diagram based on LRT, which is valid for several systems and experimental conditions, allowing us to estimate and to optimize the SPA value for a particular system.

Proposed diagram

Figure 1 presents the proposed diagram, where the axes y and x correspond to the dimensionless quantities $K_{eff}V_{mag}/k_BT$ (proportional to $\ln(\tau_N/\tau_0)$) and $\eta V_{hyd}/k_BT$ (proportional to τ_B), respectively. The main idea is the division of the diagram in different regions where the Neel relaxation, Brown relaxation, or both mechanisms are important. In this way, the curves $\tau_N = \tau_B$, $10\tau_N = \tau_B$, and $\tau_N = 10\tau_B$ are plotted. We consider two values of $\tau_0 = 10^{-9}$ s and 10^{-12} s (dashed and solid lines respectively). As expected, changes in τ_0

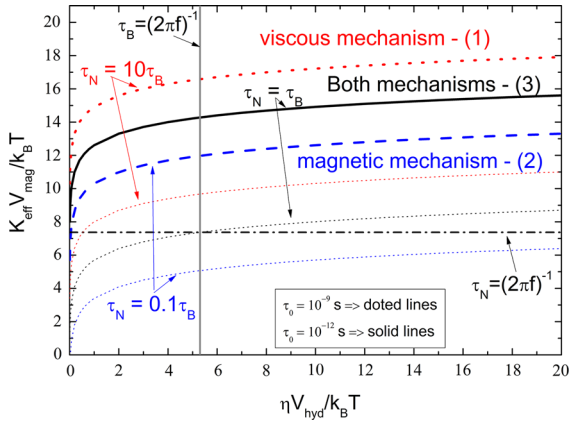

Fig. 1 Proposed diagram where y and x axes correspond to the dimensionless quantities $K_{eff}V_{mag}/k_BT$ (proportional to $\ln(\tau_N/\tau_0)$) and $\eta V_{hyd}/k_BT$ (proportional to τ_B), respectively. *Black*, *blue*, and *red lines* correspond to $\tau_N = \tau_B$, $\tau_N < 0.1\ \tau_B$ and $\tau_N > 10\ \tau_B$, respectively, when considering $\tau_0 = 10^{-9}$ and 10^{-12} s (*dashed* and *solid lines*, respectively). (Color figure online)

act as a constant proportional to $ln(\tau_0)$ that is added or subtracted to the curves. The probabilities of viscous and magnetic relaxation are proportional to $1/\tau_B$ and $1/\tau_N$, respectively, and the shorter time determines the dominant mechanism. So, the diagram can be divided in three regions: (1) $\tau_B < 0.1\tau_N$, where viscous mechanism is dominant (viscous region), (2) $\tau_N < 0.1\tau_B$, where magnetic mechanism is dominant (magnetic region), and (3) $\tau_B \sim \tau_N$, where both mechanisms play an important role. This practical diagram allows the easy estimation of the significance of each mechanism in heat generation. By knowing the main mechanism and using the proper model, it is possible to estimate the value of the SPA for the system and predict its value for different experimental conditions.

The diagram presented in Fig. 1 further contains practical relevant information: the region where the SPA value corresponding to each mechanism should be a maximum. For example, the dashed-dotted lines parallel to x and y axes correspond to the respective values of τ_N and τ_B that are equal to $1/2\pi f$ (in this case we chose $f = 300\ kHz$). Thus, the optimal SPA values are localized along these dashed-dotted lines. Hence, each line corresponds to the asymptotic value of the τ_B and τ_N where the SPA is maximum, restricted by the condition that each mechanism acts individually, without being influenced by the other.

The diagram of Fig. 1 also allows us to predict the influence of magnetic and rheological properties of a system on its SPA value according with the dominant

heating mechanism. For very low values of $K_{eff}V_{mag}/k_BT$, the Neel relaxation dominates and η and V_{hyd} are not relevant to the SPA. In addition, τ_N has an exponential dependence with $K_{eff}V_{mag}/k_BT$, and consequently the SPA dependence with this quantity will be strong, presenting a very narrow maximum. In opposition, for high values of $K_{eff}V_{mag}/k_BT$, the Brown relaxation is the dominant one and the SPA strongly depends on η and V_{hyd}. For intermediate values of $K_{eff}V_{mag}/k_BT$, where $\tau_B \sim \tau_N$, both mechanisms are relevant and the importance of each one for the heat generation is dependent on K_{eff}, V_{mag}, η, V_{hyd}, and H_0. However, in this situation the correlation between the relaxation times τ_B and τ_N must to be considered in order to understand the dominant heating mechanism. This discussion is better understood in the particular case of the ferrite nanoparticles, which are the most frequently used in MFH experiments. The effective anisotropy of ferrite systems varies in the magnitude with the composition $K_{eff} \sim 3\text{–}6 \times 10^4$ erg/cm^3 for $NiFe_2O_4$, $1\text{–}5 \times 10^5$ erg/cm^3 for Fe_3O_4 and $4\text{–}5 \times 10^6$ erg/cm^3 for $CoFe_2O_4$ (Brabers 2007, Arelaro et al. 2007, Lima et al. 2010). According to our diagram, for a usual nanoparticle size (10–30 nm), the Neel relaxation dominates for $NiFe_2O_4$, while the Brown relaxation is the dominant for $CoFe_2O_4$. For Fe_3O_4, both mechanisms are important. With respect to V_{mag}, for monodomain nanoparticles, it can be considered equal to the crystalline volume of the nanoparticles. In this work, d_{mag} is considered equal to the diameter obtained from TEM images.

In real MFH experiments involving magnetic nanoparticles, the hydrodynamic radius is generally greater than the magnetic one because of the functional layer attached to the surface of the magnetic material, generally an organic layer, which influences the relation between τ_B and τ_N. In addition, it is observed that the absorption of nanoparticles by cells and tissues leads to the formation of agglomerates (Marcos-Campos et al. 2011, Fortin et al. 2008). As a consequence, there is a drastic increment of V_{hyd} and, simultaneously, η is larger than that of the as-synthesized ferrofluids. These facts lead to the reduction in the efficiency of this mechanism of heat generation. For a system where the heat generation is dominated by Brown relaxation (according to the diagram in Fig. 1, systems with large values of K_{eff}, as $CoFe_2O_4$ nanoparticles), a drastic reduction in the value of the SPA is expected. Despite other considerations, such as the toxicity, and only considering the efficiency in the heat generation, the nanoparticle systems to be chosen for in vivo and in vitro experiments are those with an energy barrier small enough that Néel relaxation is predominant. For these systems, the large V_{hyd} and η do not play an important role in the heat generation. At the same time, the possible agglomeration during or after the internalization of the nanoparticles by the cell makes necessary to consider the interparticle interactions in order to estimate the best SPA response of the system. For moderate interparticle magnetic interaction, the value of $K_{eff}V_{mag}$ corresponding to the maximum SPA differs from the equivalent of a non-interacting system (Lima et al. 2013a,b; Branquinho et al. 2013; Mamiya 2013). As $\tau_N \propto exp(K_{eff}V_{mag})$, the dependence of the SPA with d_{mag} is very strong and presents a narrow maximum. Thus, the value of d_{mag} must be controlled with precision and the interparticle interaction must be perfectly known to obtain a large SPA for a specific value of frequency.

Validation of the diagram

In order to test the predictions of our diagram, we measure the dependence of the SPA with the frequency of the applied field for six different nanoparticle systems. Once the main heating mechanism in the diagram is identified, we use the appropriate model to calculate the SPA values as function of frequency, and these values are compared with the experimental SPA of each system. The six systems are either hydrophilic or hydrophobic nanoparticle suspensions (variation of V_{hyd} and η) of three ferrite systems with different anisotropy energy barrier distribution: Fe_3O_4 (11 nm), $CoFe_2O_4$ (13 nm), and $NiFe_2O_4$ (29 nm). The hydrophobic nanoparticles were synthesized by a chemical method similar to that described in (Arelaro et al. 2007), presenting a lognormal diameter distribution with mean diameter $d = 11$, 13, and 29 nm, and diameter dispersion $\sigma = 0.22$, 0.15, and 0.25 for Fe_3O_4, $CoFe_2O_4$, and $NiFe_2O_4$, respectively, as obtained from transmission electron microscopy images in a PHILIPS CM200 microscopy operated at 200 kV. These mean diameters were chosen in order to obtain the maximum SPA for each system.

The energy barrier distributions of these systems were obtained from magnetization measurements as function of the temperature in zero-field-cooling and field-cooling conditions (ZFC and FC curves, see Fig. 2) in a commercial SQUID magnetometer (MPMS QUANTUM DESIGNs) with $H = 100$ Oe for $CoFe_2O_4$ sample and 50 Oe for the samples $NiFe_2O_4$ and Fe_3O_4. The energy barrier distribution was obtained from the plot of $(1/T)\mathrm{d}(M_{ZFC}-M_{FC})/\mathrm{d}T$ versus T (inset of Fig. 2). For further calculations we use the mean value of the distribution. For the ZFC and FC magnetization measurements, we dispersed the nanoparticles in a polymeric matrix (PEI—polyethylenimine) in a concentration of 0.5 % *w./w.* in order to avoid the interparticle interactions. Saturation magnetization values M_S were obtained from the magnetization curves as a function of the applied field measured at $T = 300$ K in the SQUID magnetometer.

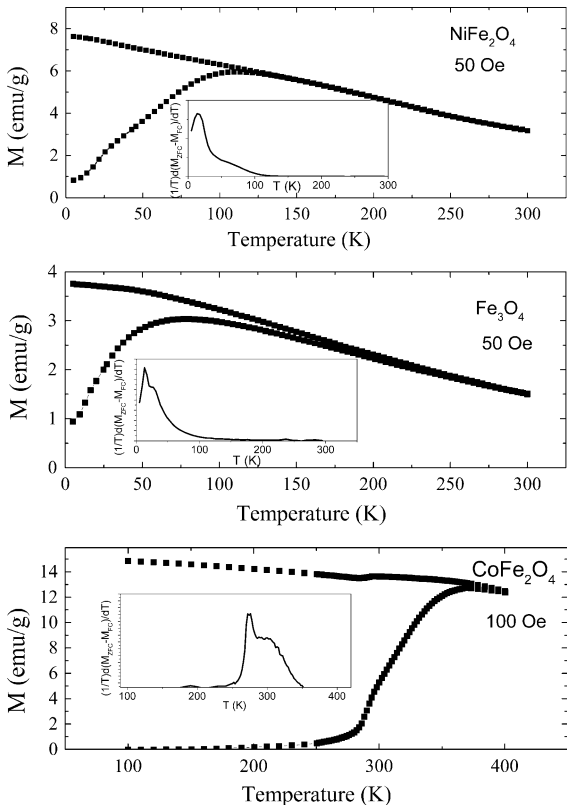

Fig. 2 Magnetization versus temperature *curves* of $CoFe_2O_4$, Fe_3O_4, and $NiFe_2O_4$ nanoparticles, measured in ZFC and FC conditions. The *insets* show the corresponding anisotropy energy barrier distribution as estimated from the $\frac{1}{T}\left[\frac{\mathrm{d}(M_{ZFC}-M_{FC})}{\mathrm{d}T}\right]$ versus T plot

Here, M_S takes into account the mass of the whole particle (magnetic core + organic layer).

The as-synthesized nanoparticles are hydrophobic, coated with an oleic acid monolayer and the hydrodynamic diameters of these samples are 20 nm (Fe_3O_4), 15 nm ($CoFe_2O_4$) and 30 nm ($NiFe_2O_4$), as measured by dynamic light scattering (DLS) in a N5 Particle Size Analyzer (Beckman and Coulter). In order to change the values of $\eta V_{hyd}/k_BT$ of these systems, the nanoparticles were turned into hydrophilic in a post-synthesis procedure. For $NiFe_2O_4$ and Fe_3O_4 systems, the hydrophilic coating was obtained by adding a phospholipid-PEG2000 conjugate that forms a bilayer with the oleic acid, while for the $CoFe_2O_4$ system it was obtained by substituting the oleic acid with PMAO (M. Moros et al. 2010). DLS measurements led to a hydrodynamic radius of hydrophilic samples of 60 nm for $CoFe_2O_4$, 50 nm for Fe_3O_4, and 70 nm for $NiFe_2O_4$.

SPA measurements were performed on a commercial equipment (DM100, nB Nanoscale Biomagnetics). The external ac magnetic field has an amplitude of $H_0 = 200$ Oe and a variable frequency $f = 229$, 355, 580, and 828 *kHz*. The SPA was obtained from the temperature versus time curves of each system by the expression $\mathrm{SPA} = (c_{liq}.m_{liq}/m_{NPs})(\mathrm{d}T/\mathrm{d}t)$, where m_{NPs} is the mass of nanoparticles, c_{liq} and m_{liq} are the specific heat and the mass of the liquid used in the experiment. The value of $\mathrm{d}T/\mathrm{d}t$ is obtained from the maximum increment rate of temperature observed in the curve of T versus *t*. The mass of the nanoparticles was measured for dry sample, thus, m_{NPs} includes the magnetic component (Fe_3O_4) and the organic layer. SPA measurements were always performed in suspensions with a concentration of 1 % w/w. of nanoparticles, which were diluted in hexane in the case of the hydrophobic systems and in water in the case of the hydrophilic ones. The experimental results for the hydrophilic and hydrophobic samples are presented in Fig. 3a–c as triangles and squares, respectively.

The diagram in Fig. 1 shows the well-known fact that the Brown relaxation is the dominant heat generation mechanism in highly anisotropic $CoFe_2O_4$ nanoparticles, whereas for Fe_3O_4 both viscous and magnetic relaxations contribute to the SPA. Accordingly, we used the LRT to simulate the dependence of the SPA on *f*, by considering $\tau_{eff}^{-1} = \tau_N^{-1} + \tau_B^{-1}$ for Fe_3O_4 (both mechanisms) and $\tau_{eff} = \tau_B$ for $CoFe_2O_4$ (viscous mechanism). The dependence of the SPA with the frequency

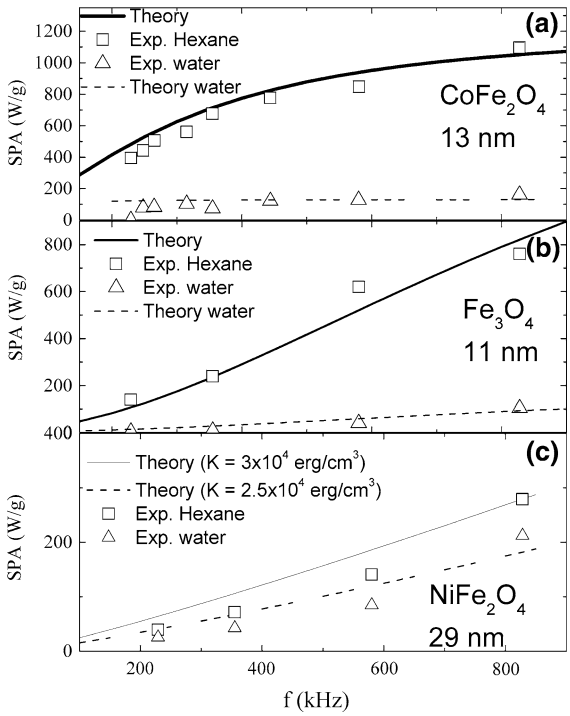

Fig. 3 **a–c** experimental (*symbols*) and calculated (*lines*) SPA values of nanoparticles of $CoFe_2O_4$, Fe_3O_4, and $NiFe_2O_4$, respectively, measured with $H_0 = 200$ Oe and $f = 229$, 355, 580, and 828 *kHz*. *Triangles* and *solid lines* correspond to hydrophobic samples, while *squares* and *dashed line* correspond to hydrophilic samples

(SPA(f)) obtained for samples in hexane and water are shown in Fig. 3a,b as solid and dashed lines, respectively. It can be noticed that the calculations are in excellent agreement with the experimental data for the two systems under different colloidal conditions. Furthermore, from the large change in the SPA values of the hydrophilic $CoFe_2O_4$ sample when compared to those of the hydrophobic one, the strong dependence of the SPA value on $\eta V_{hyd}/k_BT$ can be inferred, as corresponds to the Brown relaxation being the dominant heating mechanism. For the hydrophobic Fe_3O_4 sample, our diagram predicts that both mechanisms are important. In fact, the experimental SPA values can be well fitted with the LRT and assuming the Rosensweig model to calculate τ_{eff}. For the hydrophilic Fe_3O_4 sample, there is a strong increment in τ_B as consequence of the increment of η and V_{hyd}. Thus, the SPA of the hydrophilic Fe_3O_4 sample is basically produced by the magnetic relaxation. As a consequence, it is expected to have a small SPA value in comparison to the hydrophobic sample, in accordance with the experimental results.

For the system $NiFe_2O_4$, our diagram predicts that Néel relaxation will be the dominant one, irrespective of the $\eta V_{hyd}/k_BT$ value. Thus, the effect of the Brown relaxation will have little impact on the measured SPA values, in agreement with the experimental data shown in Fig. 3c. However, for a low-anisotropy system as $NiFe_2O_4$, the LRT framework is not appropriate to calculate the SPA under the experimental conditions of this work: the H_K value of this system, as estimated from the energy barrier and particle size distributions, is close to the maximum value of H_0 used in hyperthermia experiments (Saenger et al. 1998), and under these conditions the LRT is no longer valid for describing the relaxation process (Usov and Liubimov 2012). In addition, the comparative larger diameter of the $NiFe_2O_4$ nanoparticles increases the deviations of the experimental SPA values from the values obtained by LRT (Carrey et al. 2011; Verde et al. 2012). Therefore, for the $NiFe_2O_4$ samples the SPA was calculated as the product of the frequency and the area of the hysteresis loop of the system for a maximum field of $H_0 = 200$ Oe, which was numerically calculated as described in (Lima et al. 2013a) neglecting the interparticle interactions. We note that in this case this approximation is valid since $\tau_B > \tau_N$ for both hydrophilic and hydrophobic $NiFe_2O_4$ nanoparticles. The SPA curves simulated considering $K_{eff} = 3 \times 10^4$ and 2.5×10^4 erg/cm^3 (Fig. 3c) showed that small variations in the value of K_{eff} can strongly affect the SPA of the system when magnetic mechanism dominates. As observed, the calculated values of SPA (solid line) with $K_{eff} = 2.5 \times 10^4$ erg/cm^3 are in good agreement with the experimental ones for hydrophilic and hydrophobic samples. The difference between the SPA values of hydrophobic and hydrophilic $NiFe_2O_4$ samples, which is much smaller than the observed for the other two ferrites, can be attributed to the interparticle interactions in these samples or to a less significant contribution of the viscous mechanism to the heat generation in the case of the hydrophobic nanoparticles, with lower hydrodynamic diameter. In order to consider these effects, the SPA should be evaluated within a more complete theory than what that was used (Branquinho et al. 2013; Mamiya 2013).

According to the diagram, for the six ferrite samples, which is reinforced by our experimental results, systems with anisotropy energy barrier similar to the $NiFe_2O_4$

are the most appropriate for in vitro and in vivo MFH experiments, since the magnetic mechanism is the desirable one for this kind of experiment, where the agglomeration and the increment in the quantity $\eta V_{hyd}/k_BT$ of the particles are expected. For these systems with low-anisotropy energy, it is expected that the SPA values do not change significantly with the increment in V_{hyd} promoted by the hydrophilic character or the agglomeration. Since agglomeration of the MNPs in colloids leads to important magnetic interparticle interactions, it is thus mandatory to consider the interparticle interactions effects on the magnetic losses of these systems within an ac magnetic field with determined H_0 and f (which are important for the effects of interparticle interactions). However, other considerations must be taken into account for in vitro and in vivo MFH experiments, such as the toxicity of the nanoparticles. In this case, $NiFe_2O_4$ is not recommended and a system with similar anisotropy and lower toxicity is necessary. Different ferrites have a similar anisotropy than that of $NiFe_2O_4$ (Gonçalves et al. 2001; Verde et al. 2012). Among them, γ-Fe_2O_3 and $ZnFe_2O_4$ are best suited for in vivo magnetic hyperthermia, because they present lower toxicity than that of $NiFe_2O_4$, and recent studies have shown their potential for magnetic field hyperthermia (Verde et al. 2012; Mendoza Zelis et al. 2013).

On the other side, a system with energy barrier similar to that of $CoFe_2O_4$ is the less appropriate for in vitro and in vivo experiments, since a drastic decrease of the SPA is observed with the increase of the quantity $\eta V_{hyd}/k_BT$. Fe_3O_4 nanoparticles with small size ($\sim$10–13 nm) are also interesting candidates for in vitro and in vivo MFH experiments with moderate values of H_0. In this case, the SPA is dominated by magnetic relaxation. In addition, moderate values of SPA can be obtained for agglomerated nanoparticles with magnetic diameter of 10–15 nm for $H_0 = 150$–200 Oe (Lima et al. 2013a). These are interesting predictions from our diagram for future studies involving in vitro and in vivo experiments.

Optimization of the SPA with Linear Response Theory

Although the diagram presented on Fig. 1 is a very practical guide to determine the main mechanism of heat generation in a MFH experiment with a MNPs system characterized by the parameters V_{mag}, V_{hyd}, η, and K_{eff}, it does not determine the SPA value. Thus, we build a diagram of equipotential SPA curves in order to easily estimate and to optimize the SPA of the system as function of the relevant parameters. As mentioned before, once the main heating mechanism is identified, we need to use an appropriate model or theory to calculate the SPA value and its dependence with the characteristic parameters of the system. We consider the LRT, where the relation $M = \chi H$ is assumed, which is valid when the anisotropy field (H_K) is higher enough than H_0. This assumption is valid for the region in the diagram where the Brown mechanism dominates (region (1)) independently of the value of H_0, and it is also valid for the region (3) ($\tau_B \sim \tau_N$) if we consider the typical values of H_0 used in the hyperthermia experiments. For region (2), where magnetic mechanism is dominant, the validity of this assumption depends on the value of H_0 in comparison to H_K. The most important parameter in the LRT is the effective relaxation time (τ_{eff}). In the region (1), τ_{eff} can be considered equal to τ_B. For region (3), where the use of LRT is conditioned by the value of H_0, τ_{eff} can be considered equal to τ_N. For region (2), where both Brown and Néel relaxation mechanisms are relevant, the effective relaxation time is more difficult. According to Rosensweig's model (Rosensweig 2002), both mechanisms are independent and take place in parallel, consequently τ_{eff} can be easily defined: $\tau_{eff}^{-1} = \tau_B^{-1} + \tau_N^{-1}$. Despite the limitations of this model (Haiwen Xi et al. 2006), it can give a correct description in the limits where each mechanism is dominant. In addition, the region where both mechanisms coexist is relatively small (due to the exponential dependence of τ_N with $K_{eff}V_{mag}/k_BT$) and the continuity of the time functions makes that the actual relaxation time does not differ much from that calculated by Rosensweig's model. In fact, there are experimental results reported in the literature (Kallumadil et al. 2009, Lima et al. 2013b, Gonzales-Weimuller et al. 2009, Eggeman et al. 2007) that are relatively well fitted with Rosensweig's model.

We based the diagram of equipotential SPA curves on three main assumptions: (i) non-interacting nanoparticles system, (ii) the validity of the LRT, *i.e.* the anisotropy field H_K is greater than the ac applied field H_0, and (iii) magnetic relaxation mechanisms (Néel and Brown relaxations) are independent and take place

in parallel (Rosensweig's model). According to the LRT, the SPA is given by: $SPA = \pi\chi_0 f H_0^2 2\pi f \tau_{eff} / (1 + (2\pi f \tau_{eff})^2)$, where χ_0 is the initial susceptibility of the system. Calling $u = \tau_f/\tau_{eff}$ (where $\tau_f = 1/2\pi f$ is the inverse of the angular frequency of excitation), a reduced expression of SPA can be written:

$$S = 2u/(1 + u^2), \tag{1}$$

where $S = SPA/SPA_M$ and $SPA_M = \pi H_0^2 f \chi_0/2$ is the highest SPA value.

The diagram of equipotential SPA curves is presented in Fig. 4a. It was constructed by using as variables $x = \tau_f/\tau_B$ and $y = \tau_f/\tau_N$ in a logarithm scale for simultaneous visualization of those samples with coordinates that span a wide range of x, y values. The curve where $SPA = SPA_M$ (or $S = 1$) corresponds to the red solid line. The plotted green dashed curve corresponds to Eq (1). As an example, we used the coordinates $(x_0,y_0) = (2,3)$ (symbol * in the Fig. 4, on the dotted blue line). With these coordinates, we calculated the value $u_0 = x_0 + y_0 = 5$, and according to Eq. (1) we obtained $S \sim 0.38$.

In addition, the diagram of equipotential SPA curves of Fig. 4a easily gives the optimal frequency (f^*) for the maximum SPA for a system with a determined u_0 value. This frequency is given by $f^* = u_0 f$. In other words, if we perform an experiment at $f = f^*$, the point (x_0,y_0) becomes (2/5,3/5), and then in the new diagram it "points out" at the optimum curve $S = 1$. From this example it is evident that if the u_0 value is greater/lower than 1, it would be necessary to increase/decrease the frequency of the experimental setup in order to get the optimal S value. In some cases it could be very difficult to change the operation frequency of the experiment, and the only way to obtain the maximum SPA would be to tune the the sample parameters (V_{mag}, V_{hyd}, K_{eff}, and η) in order to work at the ideal condition.

In order to test the usefulness of the proposed equipotential diagram, we apply it to hydrophobic and

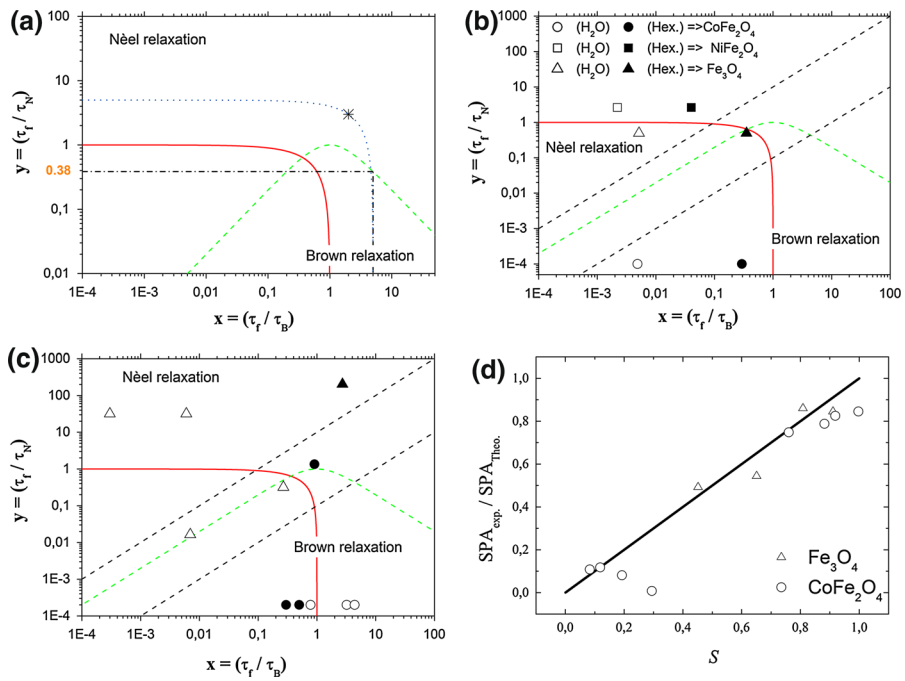

Fig. 4 **a**, **b**, **c** Diagrams of equipotential SPA *curves* ($x = \tau_f/\tau_B$ vs. $y = \tau_f/\tau_N$). In **a**, the *dotted blue line* is the *curve* of the equipotential surface corresponding to the hypothetical point with $(x_0,y_0) = (2,3)$ (*), which is used as example. In **b**, symbols correspond to the (x,y) experimental values for our nanoparticles: Fe_3O_4 (11 nm), $CoFe_2O_4$ (13 nm), and $NiFe_2O_4$ (29 nm). In **c**, symbols (x,y) correspond to experimental values for Fe_3O_4, $CoFe_2O_4$, and $NiFe_2O_4$ nanoparticles presented in the literature (*triangle* in (Kallumadil et al. 2009), *filled triangle* in (Eggeman et al. 2007), *circle* in (Lee et al. 2011), and *filled circle* in (Torres et al. 2010)). The *curve* where $SPA = SPA_M$ (or $S = 1$) corresponds to the *red solid line*. The *plotted green dashed curve* corresponds to Eq (1). **d** Normalized experimental SPA value versus the theoretical one (S) for our Fe_3O_4 (*filled triangle* and *triangle*) and $CoFe_2O_4$ (*filled circle* and *circle*) nanoparticles. (Color figure online)

hydrophilic ferrite nanoparticles case. Figure 4b presents the values of x and y for nanoparticles of $CoFe_2O_4$ (13 nm), Fe_3O_4 (11 nm), and $NiFe_2O_4$ (29 nm) plotted on the diagram of Fig. 4a. In order to calculate V_{hyd}, we have considered an organic layer of 2 nm thickness for the hydrophobic nanoparticles (solid symbols) and a layer of 20 nm thickness for the hydrophilic nanoparticles (open symbols), and we used $\eta = 0.03$ and 0.1 g/cm.s, respectively. The measured length of the oleic acid chain is about 2 nm (Zhang et al. 2006), and that is why this value has been used in the calculations. For the hydrophilic coatings (PE-mPEG2000 and PMAO), it is more difficult to use reference lengths to calculate the thickness of the coating, since the morphology of the molecule may change. Therefore, we decide to use values close to the experimental ones obtained from DLS measurements. Finally, we used a frequency of 580 kHz for the applied field.

As observed in Fig. 4b, the values corresponding to the $CoFe_2O_4$ nanoparticles with both coatings are localized in Brown relaxation region, which means that the Brown relaxation mechanism dominates the SPA of both samples. In opposition, the values corresponding to the hydrophobic and hydrophilic $NiFe_2O_4$ nanoparticles are in the Néel relaxation region, so Néel relaxation mechanism plays the fundamental role in the SPA. The main heating mechanism for hydrophilic Fe_3O_4 nanoparticles is the Néel relaxation, while for the hydrophobic nanoparticles both Néel and Brown relaxations are important.

Other noteworthy feature observed in Fig. 4b is that the values corresponding to the three hydrophobic systems are close to the curve $SPA = SPA_M$, indicating that these nanoparticles have the most suitable magnetic parameters to obtain the best response in terms of SPA, always taking into account whether the LRT is valid or not (specially for the Ni Ferrite). However, the hydrophilic systems present different features: the SPA expected for the $CoFe_2O_4$ system is much smaller than expected; the point (x,y) of Fe_3O_4 nanoparticle system presents a disruption from the curve $SPA = SPA_M$, indicating a reduction in the SPA of the hydrophilic Fe_3O_4 system.

The proposed diagram of equipotential surfaces is totally valid in the frequency range typically used in an MFH experiment, since the power absorption mechanisms for a magnetic nanoparticle colloid will not vary if the frequency is in the range of 50–900 kHz; for any of these values the lines delimiting the regions of validity of the SPA mechanisms will be parallel to the black dashed lines in the diagram.

Figure 4c gives the SPA (x and y values) in the diagram for different ferrite samples presented in the literature: Fe_3O_4 (Δ by (Kallumadil et al. 2009) and ▲ by (Eggeman et al. 2007)) and $CoFe_2O_4$ (○ by (Lee et al. 2011) and • by (Torres et al. 2010)). As observed, both the Néel and Brown mechanisms play a role in the case of samples of Fe_3O_4, with a maximum SPA expected for nanoparticles of 11–13 nm magnetic diameter and about 15 nm of hydrodynamic diameter. In the case of $CoFe_2O_4$, the main dominant mechanism is always the viscous one, with an optimal performance for hydrodynamic diameter about 12–16 nm. The maximum magnetic response is found for $CoFe_2O_4$ nanoparticles with a magnetic diameter of 5 nm, with a maximum SPA significantly lower than that observed for 12–16 nm where viscous mechanism dominates.

Figure 4d plots the comparison between the experimental SPA values of our hydrophilic and hydrophobic $CoFe_2O_4$ and Fe_3O_4 nanoparticles (presented in Fig. 3a,b, respectively), normalized by the calculated SPA_M, versus the expected value of S given by Eq. (1) (i.e., it represents SPA_{exp}/SPA_M vs. S). SPA_M and S were calculated by using the parameters measured for our samples (the mean blocking temperature $< T_B >$, V_{hyd} and M_S, given in Table 1) and assuming $\tau_0 = 10^{-10}$ s and the tabulated values of viscosity η for the hexane and water. If SPA_{exp} values are close to the predicted ones of the diagram of equipotential SPA curves, then $SPA_{exp}/SPA_M = S$. This relation is represented as the solid line in the graphic and it corresponds to the prediction of the LRT for the SPA of our nanoparticles. As expected, the values for $CoFe_2O_4$ and Fe_3O_4 systems fit very well with the predicted values (close to the solid line). Thus, the diagram of Fig. 4a is able to predict the SPA value of our Fe_3O_4 and $CoFe_2O_4$ nanoparticles suspension, and we can use this diagram to determine the experimental conditions in order to optimize the SPA. In our case, the hydrophobic Fe_3O_4 and $CoFe_2O_4$ nanoparticles have diameters that lead to a SPA close to the maximum. We have not plotted the values for $NiFe_2O_4$ nanoparticles, because the LRT is not valid for this system for the frequency values used in the experiment.

Table 1 Parameters used to calculate the theoretical SPA in Fig. 3: mean blocking temperature $< T_B >$ (obtained from the ZFC and FC magnetization measurements); saturation magnetization M_S (obtained from M(H) measurements); V_{hyd} (obtained from DLS measurements); the viscosity η of water and hexane (tabulated), and the value of τ_0 (tabulated)

Sample	$<T_B>$ (K)	M_S (emu/g)	V_{hyd} (nm)	η (cP)	τ_0 (s)
$NiFe_2O_4$ (H_2O)	16	48	70	1.00	10^{-10}
$NiFe_2O_4$ (Hexane)	16	48	30	0.31	10^{-10}
$CoFe_2O_4$ (H_2O)	370	63	60	1.00	–
$CoFe_2O_4$ (Hexane)	370	63	15	0.31	–
Fe_3O_4 (H_2O)	22	70	50	1.00	10^{-10}
Fe_3O_4 (Hexane)	22	70	20	0.31	10^{-10}

Conclusions

In summary, we have developed a SPA diagram that can be used to foresee the heating mechanism of single-domain magnetic nanoparticles suspensions, before they are used in MFH experiments. This diagram takes into account the viscous (Brown) and magnetic (Neél) relaxation times of the system, and that the heating mechanism depends on the parameters $K_{eff}V_{mag}/k_BT$ and $\eta V_{hyd}/k_BT$. By this diagram, the main heating mechanisms for a particular nanoparticles system can be inferred. We have verified this approach on samples with different magnetic and physicochemical properties. For magnetic colloids composed of $CoFe_2O_4$ nanoparticles, we have demonstrated that the "*viscous relaxation*" and thus the SPA strongly depend on η and V_{hyd}. For $NiFe_2O_4$-based colloids, the "*magnetic relaxation*" has been found to dominate, making the SPA independent of η and V_{hyd}, but strongly dependent on $K_{eff}V_{mag}/k_BT$. For the Fe_3O_4 system, the main heating mechanism depends on the values of η and V_{hyd}; magnetic mechanism dominates for high values of ηV_{hyd}, while both mechanisms are important for low values of these parameters. In fact, these predictions are confirmed by the measurements of SPA values of hydrophobic and hydrophilic ferrite nanoparticles as a function of the ac magnetic field frequency. Fe_3O_4 hydrophilic system presents a reduction in the SPA in comparison with that measured for the Fe_3O_4 hydrophilic sample. However, significant values of SPA can be obtained for this system for moderate values of H_0 ($\sim$200 Oe). Our results suggest that $CoFe_2O_4$ nanoparticle systems are not suitable for MFH since a strong reduction in the SPA is expected for agglomerated and interacting nanoparticles in in vitro and in vivo MFH experiments. We also proposed a diagram of equipotential SPA curves based on the LRT and on the Rosensweig's model, which allows us to estimate the SPA value for a system with a simple calculation. This diagram also gives us visual information in order to tune f for obtaining an optimum SPA. Our results presented here have a range of validity, especially the diagram for predicting the heating mechanisms and the diagram of equipotential curves. First of all, both of them refer to non-interacting systems, i.e., without magnetic interparticle interactions. In the specific case of the diagram of equipotential curves, for the optimization of the SPA, the calculations are based on the LRT. In addition, for the region where both mechanisms, Neel and Brown relaxation, play an important role we have made the approximation of assuming that both mechanisms are independent and take place in parallel.

Acknowledgments The authors are grateful to the CONICET-Argentina. The authors would also like to acknowledge the use of the Servicio General de Apoyo a la Investigación – SAI, Universidad de Zaragoza. This work was supported partially from the Argentinean agencies ANPCyT (PICT2007-832), CONICET (PIP2008-1333), and UNCuyo grants. This work also was supported from Diputación General de Aragon (DGA) and Ministerio de Economia y Competitividad (MINECO, Project MAT2010-19326) - Spain.

Conflict of interest The authors declare no conflict of interest in the results presented in this article.

References

Arelaro AD, Lima E Jr, Rossi LM, Kiyohara PK, Rechenberg HR (2007) Ion dependence of magnetic anisotropy in MFe2O4 (M = Fe Co, Mn) nanoparticles synthesized by high-temperature reaction. J Magn Magn Mater 320:e335–e338

Brabers VAM (2007) Ferro- and ferrimagnetic oxides and alloys. In: Kronmüller H, Parkin S (eds) Handbook of magnetism and advanced magnetic materials, vol 1. John Wiley & Sons, New York cap. 9

Branquinho LC, Carriao MS, Costa AS, Zufelato N, Sousa MH, Miotto R, Ivkov R, Bakuzis AF (2013) Effect of magnetic dipolar interactions on nanoparticle heating efficiency: implications for cancer hyperthermia. Sci Rep 3:2887

Brezovich IA (1988) Low frequency hyperthermia: Capacitive and ferromagnetic thermoseed methods. In: Palival PR, Hetzel FW (eds) Medical physics monograph, vol 16. American Institute of Physics, New York, p 82

Carrey J, Mehdaoui B, Respaud M (2011) Simple models for dynamic hysteresis loops calculation: application to hyperthermia optimization. J Appl Phys 109:083901

Eggeman AS, Majetich SA, Farrell D, Pankhurst QA (2007) Size and concentration effects on high frequency hysteresis of iron oxide nanoparticles. IEEE Trans Magn 43: 2451–2453

Fortin JP, Gazeau F, Wilhelm C (2008) Intracellular heating of living cells through Néel relaxation of magnetic nanoparticles. Eur Biophys J 37:223–228

Gonçalves GRR, Pereira AR, Bakuzis AF, Skeff Neto K, Pelegrini F, Morais PC (2001) Magnetic resonance of zinc- and copper-ferrite ionic magnetic fluids: temperature effects. J Magn Magn Mater 226–230:1896–1898

Gonzales-Weimuller M, Zeisberger M, Krishnan KM (2009) Size-dependant heating rates of iron oxide nanoparticles for magnetic fluid hyperthermia. J Magn Magn Mater 321:1947–1950

Kallumadil M, Tada M, Nakagawa T, Abe M, Southern P, Pankhurst QA (2009) Suitability of commercial colloids for magnetic hyperthermia. J Magn Magn Mater 321: 1509–1513

Laurent S, Dutz S, Häfeli UO, Mahmoudi M (2011) Magnetic fluid hyperthermia: focus on superparamagnetic iron oxide nanoparticles. Adv Colloid Interface Sci 166:8–23

Lee JH, Jang JT, Choi JS, Moon SH, Noh SH, Kim JW, Kim JG, Kim IS, Park KI, Cheon J (2011) Exchange-coupled magnetic nanoparticles for efficient heat induction. Nature Nanotech 6:418–422

Lima E Jr, De Biasi E, Mansilla MV, Effenberg F, Rossi LM, Cohen R, Rechenberg HR, Zysler RD (2010) Surface effects in the magnetic properties of crystalline 3 nm ferrite nanoparticles chemically synthesized. J Appl Phys 108: 103919

Lima E Jr, De Biasi E, Mansilla MV, Mojica Pisciotti ML, Saleta ME, Granada M, Troiani HE, Effenberg FB, Rossi LM, Zysler RD (2013a) Heat generation in agglomerated ferrite nanoparticles in an alternating magnetic field. J Phys D Appl Phys 46:045002

Lima E Jr, Torres TE, Rossi LM, Rechenberg HR, Berquo TS, Ibarra A, Marquina C, Ibarra RM, Goya GF (2013b) Size dependence of the magnetic relaxation and specific power absorption in iron oxide nanoparticles. J Nanopart Res 15:1654

Maier-Hauff K, Rothe R, Scholz R, Gneveckow U, Wust P, Thiesen B, Feussner A, von Deimling A, Waldoefner N, Felix R, Jordan A (2007) Intracranial thermotherapy using magnetic nanoparticles combined with external beam radiotherapy: results of a feasibility study on patients with glioblastoma multiforme. J Neurooncol 81:53–60

Mamiya H (2013) Recent advances in understanding magnetic nanoparticles in AC magnetic fields and optimal design for targeted hyperthermia. J Nanomater. 752973

Mamiya H, Jeyadevan B (2011) Hyperthermic effects of dissipative structures of magnetic nanoparticles in large alternating magnetic fields. Sci Rep 1:157

Marcos-Campos I, Asín L, Torres TE, Marquina C, Tres A, Ibarra RM, Goya GF (2011) Cell death induced by the application of alternating magnetic fields to nanoparticle-loaded dendritic cells. Nanotechnology 20:205101

Mendoza Zelis P, Pasquevich GA, Stewart SJ, Fernandez van Raap MB, Aphesteguy J, Bruvera IJ, Laborde C, Pianciola B, Jacobo S, Sanchez FH (2013) Structural and magnetic study of zinc-doped magnetite nanoparticles and ferrofluids for hyperthermia applications. J Phys D Appl Phys 46:125006

Moros M, Pelaz B, Lopes-Larrubia P, Garcia-Martin ML, Grazu V, de la Fuente JM (2010) Engineering biofunctional magnetic nanoparticles for biotechnological applications. Nanoscale 2:1746–1755

Rosensweig RE (2002) Heating magnetic fluid with alternating magnetic field. J Magn Magn Mater 252:370–374

Saenger JF, Skeff Neto K, Morais PC, Sousa MH, Tourinho FA (1998) Investigation of the anisotropy in frozen nickel ferrite ionic magnetic fluid using magnetic resonance. J Magn Res 134:180–183

Torres TE, Roca AG, Morales MP, Ibarra A, Marquina C, Ibarra MR, Goya GF (2010) Magnetic properties and energy absorption of $CoFe_2O_4$ nanoparticles for magnetic hyperthermia. J Phys 200:072101

Usov NA, Liubimov BYa (2012) Dynamics of magnetic nanoparticle in a viscous liquid: application to magnetic nanoparticle hyperthermia. J Appl Phys 112:023901

Verde EL, Landi GT, Carrião MS, Drummond AL, Gomes JA, Vieira ED, Sousa MH, Bakuzis AF (2012) Field dependent transition to the non-linear regime in magnetic hyperthermia experiments: Comparison between maghemite, copper, zinc, nickel and cobalt ferrite nanoparticles of similar sizes. AIP Adv 2:032021

Xi H, Gao K-Z, Shi Y, Xue S (2006) Precessional dynamics of single-domain magnetic nanoparticles driven by small ac magnetic fields. J Phys D Appl Phys 39:4746–4752

Zhang L, He R, Hong-Chen Gu (2006) Oleic acid coating on the monodisperse magnetite nanoparticles. Appl Surf Sci 253:2611–2617